Journal of the Brazilian Society of Mechanical Sciences and Engineering (2021) 43:97
https://doi.org/10.1007/s40430-021-02822-y

TECHNICAL PAPER

Numerical investigation of dynamic stall reduction on helicopter blade section in forward flight by an airfoil deformation method

S. M. H. Karimian[1] · S. V. Aramian[1] · Abolfazl Abdolahifar[1]

Received: 27 June 2020 / Accepted: 9 January 2021 / Published online: 29 January 2021

Abstract

In the present work, airflow over blade section of helicopter rotor in forward flight is investigated numerically to offer a proposal for reduction or alleviation of dynamic stall on retreating blade. Unsteady 2-D compressible Reynolds-averaged Navier–Stokes equations are solved at flow conditions experienced by retreating blade of UH-60A helicopter rotor. For validation and verification purposes, flows around static and pitching airfoils in constant and variable flow Mach numbers are simulated and compared with other numerical results and experimental data. Having defined two deformation parameters, nine different permanently-deformed airfoils are produced from SSC-A09 airfoil. Flow field around these nine airfoils are simulated in variable flow Mach number with defined pitching angles. Coefficients of C_l, C_d and C_m of these deformed SSC-A09 airfoils are compared with those of original airfoil to demonstrate that airfoil deformation proposed here is able to reduce and alleviate dynamic stall. Quantitatively, $C_{d,max}$ and absolute value of $C_{m,min}$ have been reduced up to 49.2% and 25%, respectively. In addition it is worth to mention that in some flow conditions dynamic stall is even eliminated with the proposed airfoil deformation. These are all achieved by permanent airfoil deformation which does not impose design complexities and expenses needed by dynamic airfoil deformation as proposed by others.

Keywords Dynamic stall · Helicopter · Forward flight · Airfoil drooping · Rotor blade · Numerical simulation

List of symbols

c	Airfoil chord
C_d	Section drag coefficient (−)
C_l	Section lift coefficient (−)
C_m	Section pitching moment coefficient (−)
C_P	Pressure coefficient (−)
dt_0	Time step (s)
M	Local Mach number (−)
M_∞	Helicopter Mach number, free-stream Mach number (−)
r	Section radius along the rotor blade
R	Blade radius
r/R	Non-dimensional blade radius (−)
Re	Reynolds number (−)
V_∞	Free-stream velocity
$x/c,\ y/c$	Non-dimensional coordinates measured from airfoil leading-edge (−)
y^+	Dimensionless wall distance (−)

Abbreviations

CFD	Computational fluid dynamics
DD	Dynamically-deformed
PD	Permanently-deformed
RANS	Reynolds-averaged Navier Stokes
RPM	Revolution per minute
2-D	Two-dimensional
3-D	Three-Dimensional

Greek letters

α	Section angle of attack (°)
θ	Section droop angle (°)
μ	Advance ratio $= V_\infty/R\omega$ (−)
ψ	Azimuth angle (°)
ω	Rotor angular velocity

Technical Editor: André Cavalieri.

✉ S. M. H. Karimian
hkarim@aut.ac.ir

S. V. Aramian
v.aramian@aut.ac.ir

Abolfazl Abdolahifar
a.abdolahifar@aut.ac.ir

[1] Department of Aerospace Engineering, Amirkabir University of Technology (Tehran Polytechnic), 424 Hafez Avenue, P.O. Box: 15875-4413, Tehran, Iran

Subscripts

cr	Center of rotation on airfoil camber
ls	Lift stall
L.E.	Airfoil leading-edge
N	New camber point
P	Point on airfoil camber

1 Introduction

At high forward speeds, performance of rotorcraft is limited by dynamic stall in retreating blade, and depending on the airfoil design by the compressibility effects in the advancing blade. Since advancing and retreating rotor blades experience different airflows on the blade section of rotorcraft, blade angle of attack should vary cyclically to balance lift force and prevent roll-fluctuations of rotorcraft. Low speed airflow occurs on the retreating blade where rotational speed of blade section and flight speed of rotorcraft become in the same direction. As a result, retreating blade should perform at high angles of attack especially close to azimuth angle of 270°. Obviously, this causes dynamic stall and reduces aerodynamic performance of the rotor blade. This is why the objective of many types of research is to reduce or alleviate dynamic stall.

Dynamic stall has been studied experimentally [1–9] and numerically [7, 9–13]. In addition, there are some semi-empirical dynamic stall models predicting aerodynamic coefficients of airfoils, such as work of Sadr et al. [14].

Numerical studies are carried out both in two and three dimensions. It is well known that rotorcraft flight envelope can be extended by reduction, alleviation or elimination of dynamic stall. Studies have been carried out in the literature for dynamic stall reduction by means of flow control. These include using vortex generators [15–17], deformation of airfoil leading-edge [18–23], employment of zero mass jets [24], installation of airfoil leading or trailing-edge flaps [25, 26], and employment of fluid blowing and sucking devices [27]. For instance, in 2018, Al-Jaburi and Feszty [17] proposed 26 different geometry modifications to form trapped-vortex generator on NACA-0012 pitching airfoil. Having simulated flow field around these cases two-dimensionally, they were able to reduce peaks of negative pitching moment, drag and lift for about 37–63%, 14–38% and 2–8%, respectively.

Among flow control methods developed to reduce or alleviate dynamic stall, focus of the present study is on the deformation or drooping of the airfoil leading-edge in forward flight of rotorcraft.

In 2001, Reuster and Baeder [22] used 2-D numerical simulation to show that dynamic nose drooping of airfoil reduces drag and moment coefficients during dynamic stall in constant Mach number. Nose drooping implemented in Ref. [22] is a function of leading-edge pressure coefficient. Non-smooth airfoil surface is observed in geometries reported in Ref. [22], since nose drooping has not been implemented continuously. In 2003, Sahin et al. [21] studied effect of airfoil nose radius on the dynamic stall by 2-D numerical simulation of flow field around airfoil in constant Mach number of 0.3 and sinusoidal angle of attacks. In this work, leading-edge radius of the airfoil increases dynamically at high angles of attack. As a result, it was observed that pitching moment, lift and drag hysteresis loops were milder for the dynamically-deformed (DD) airfoil compared to that of baseline airfoil. They also compared results of this DD airfoil with results of permanently-deformed (PD) airfoil based on the largest nose radius and concluded that for this nose radius PD airfoil performs as well as DD airfoil. In 2012, 2-D numerical simulations carried out by Ramesh et al. [18] also confirmed that higher nose radius delays flow separation on pitching airfoil at constant flow Mach numbers. In 2015 Wang et al. [28] proposed a permanent airfoil, reshaped by implementation of an optimization algorithm incorporating an unsteady 2-D CFD code. With this new shape of airfoil, peak values of drag and pitching moment coefficients were reduced by nearly 80% during the dynamic stall cycle at constant Mach flow and sinusoidal angle of attacks. In 2018, Benton and Visbal [29] analysed effects of leading-edge geometry on the onset of dynamic stall of a pitching NACA-23012 airfoil. They concluded that increase of the leading-edge radius and addition of leading-edge droop could delay the onset of dynamic stall. In 2018, Niu et al. [30] implemented a variable leading-edge droop on an oscillating NACA-0012 airfoil in their 2-D numerical simulation to reduce dynamic stall. In this method, local angle of attack near the leading-edge dynamically decreases when the overall angle of attack gets too large. In one case, leading-edge drooping resulted in 61% increase in lift, 81% decrease in drag and 69% decrease in amplitude variation of pitching moment during one period. Other similar works using variable leading-edge drooping can be found in the literature, e.g., the work of Zhao and Zhao [31]. However, it should be noted that variable leading-edge drooping adds complexity to the whole system and increases its cost.

Note that all of the above cases were at constant Mach number. In fact, performance of airfoils in these studies is in question if the local Mach number is variable due to the forward flight of helicopter. There are few prominent and relevant types of research which consider effects of rotorcraft forward flight velocity.

In 2002, Babinsky and Fernie [32] ran experiments on a static airfoil in unsteady flow with variable flow Mach numbers in the range of forward flight speeds of helicopters to analyse aerodynamics of helicopter blade section. In this work, effects of helicopter acceleration and deceleration on aerodynamic characteristics of advancing and

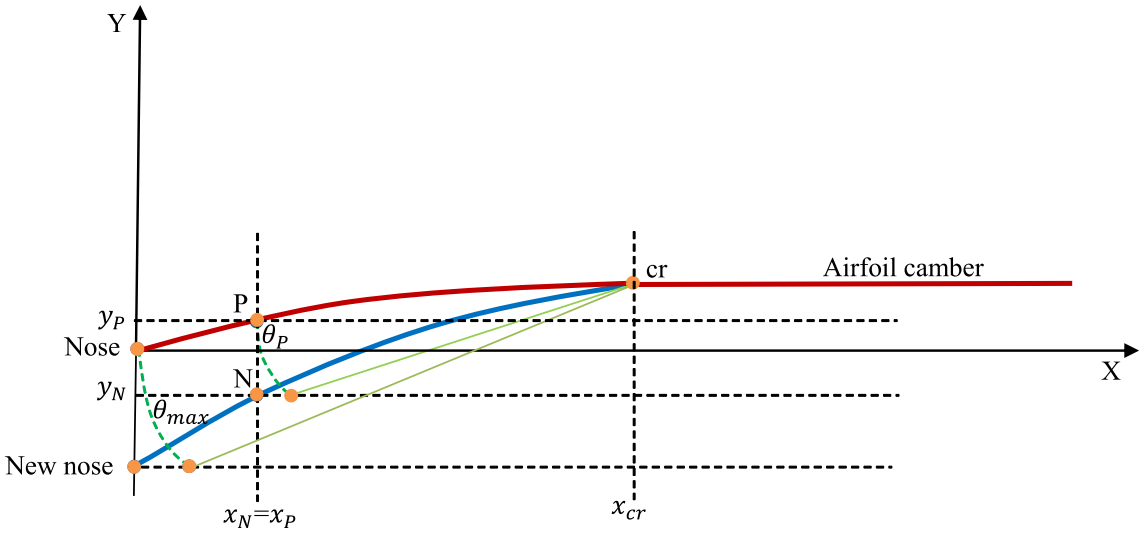

Fig. 1 Schematic of camber deformation parameters

retreating airfoils are investigated. It was shown that the shock wave terminating supersonic region is less intense during the accelerating part of the cycle compared to that of the decelerating part. The 2-D work of Huang et al. [33] in 2015 which focuses on aerodynamic force and moment coefficients, concludes that flow with variable velocity significantly affects airfoil aerodynamics especially the lift coefficient. In 2017, Zhao et al. [34] improved unsteady aerodynamic characteristics of an oscillating airfoil in forward flight, using synthetic jet located on the upper surface of rotor blade. Therefore, it seems that consideration of variable velocity or Mach number in dynamic stall analysis of helicopter blade is inevitable.

Note that shock waves may occur on an airfoil for Mach numbers as low as 0.2 if the angle of attack is sufficiently high [13, 35]. Therefore, although shock waves are not expected generally in retreating blade Mach numbers, care should be taken in the analysis of rotor blades even at low Mach numbers.

A more realistic study is done by Kerho [19] who studied cases with variable flow Mach number due to helicopter forward flight at angles of attack near to practical condition using rotorcraft blade analysis code of CAMRAD II [36]. Using 2-D numerical simulation, it was shown that dynamic nose drooping has alleviated dynamic stall of SSC-A09 airfoil and reduces extreme values of drag and moment coefficients in dynamic stall region. Larger $C_{l,max}$ is produced by the SSC-A09 airfoil at near stall angles at the expense of drag and negative pitching moment increase at lower angles of attack. Breaks in the C_d and C_m curves occur at a significantly lower α for the SSC-A09 airfoil as compared with the deformed airfoil (15–17° as compared with 19.6°). These breaks denote formation of dynamic stall vortex and their passing into the downstream.

Dynamic deformation of helicopter blade section imposes significant amount of complexity in structure and control system of blade. It also adds to the weight of the blade. From this point of view, it is obvious that a permanently-deformed airfoil is preferred. Therefore, the objective of the present study is to propose an airfoil deformation method with smooth nose drooping to reduce, alleviate or eliminate dynamic stall of helicopter blade section in variable flow Mach numbers. Three-dimensional numerical simulation is the first choice of any researcher

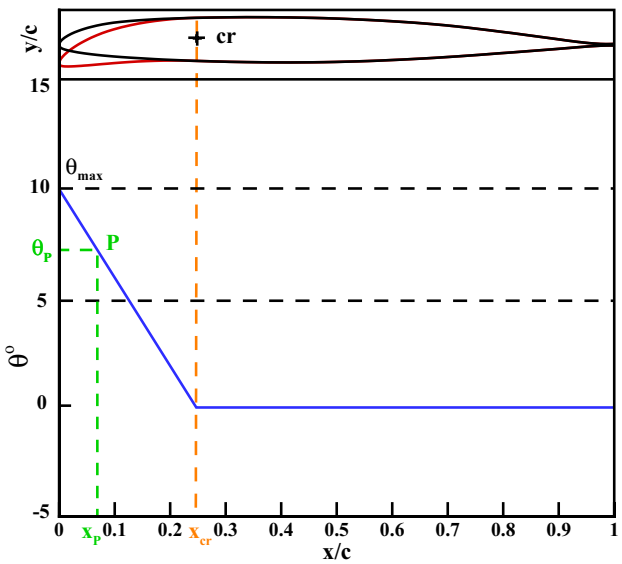

Fig. 2 Variation of θ_P with $\frac{x}{c}$ for $\theta_{max} = 10°$ and $x_{cr}/c = 0.247$

if computational cost is not an issue. Nevertheless, two-dimensional simulation has been used also by many researchers in Refs. [17–19, 21, 22, 28, 30, 31, 33, 34, 37, 38] to investigate dynamic stall. This is because with much less computational efforts two-dimensional simulation produces results with acceptable accuracy. Following the literature and based on the computational resources available for the authors, 2-D numerical simulation will be used in the present work. Results obtained by Kerho [19] will be used as the main reference for verification in the present work.

Table 1 Different grids employed for the grid convergence study

No.	Grid	Nodes on the airfoil	Structured cells	Unstructured cells	Total cells
1	Grid-I	600	84,741	24,091	108,832
2	Grid-II	800	112,941	41,160	154,101
3	Grid-III*	1000	141,141	46,610	187,751
4	Grid-IV	1200	168,140	49,289	217,429

*Grid finally chosen in present work

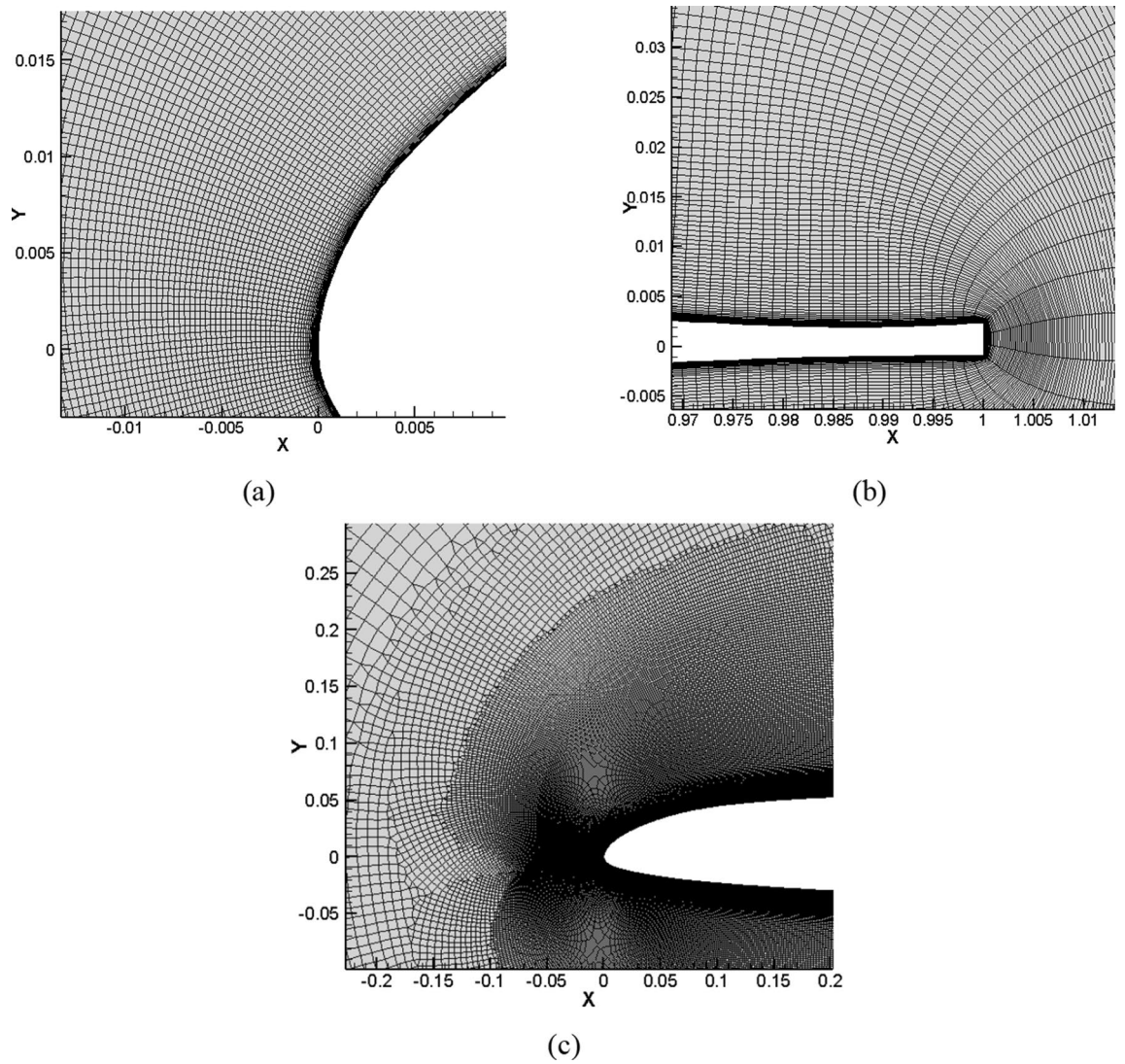

Fig. 3 Computational grid: **a** structured region near airfoil leading-edge, **b** structured region near airfoil trailing-edge and **c** grid transition from structured to unstructured

2 Numerical method

Flow field around of helicopter blade section is simulated by the solution of two-dimensional unsteady compressible turbulent flow using RANS equations. Spalart–Allmaras turbulence model designed specifically for aerospace applications performs very well in the presence of adverse pressure gradient; for more details about turbulence transport equation see Ref. [39]. One-equation Spalart–Allmaras turbulence model has been successfully used by different researchers including Kerho [19], Wang and Zhao [40] and Zhao and Zhao [31]. Following the work of these researchers, this turbulence model is used to simulate turbulent flow in the present study, as well. Mass, momentum and energy conservation equations are solved coupled to each other, but turbulence equation is solved in a segregative manner. In this method inviscid flux terms are calculated using ROEs flux-splitting method [41].

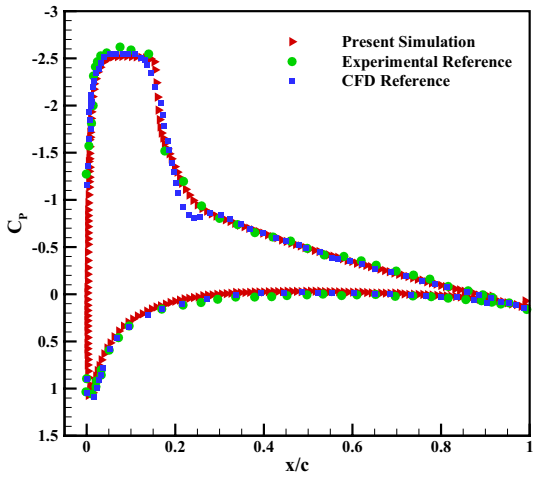

Fig. 5 Surface pressure coefficient compared to experimental data and numerical results of Ref. [12] at $M = 0.6$ and $\alpha = 6.48°$ (static airfoil)

3 Geometry and grid

Airfoils used in this study are NACA-0012 and SSC-A09. NACA-0012 airfoil is used for numerical validation and SSC-A09 airfoil employed at radius $r/R = 0.865$ of rotor blade section of UH-60A Blackhawk helicopter, is used for numerical verification. Note that all numerical studies in this paper will be performed on SSC-A09 airfoil.

Airfoil deformation method used in present work is described in Fig. 1. Consider a point called P on the camber of original airfoil with coordinates of x_P and y_P. New y-coordinate of this point after airfoil deformation, denoted by y_N, is determined by the rotation of point P around point cr on the airfoil camber, equal to θ_P. Radius of this rotation is the distance between points P and cr. In addition $\theta_P = \left(\left(x_{cr} - x_P\right)/x_{cr}\right)\theta_{max}$, where x_{cr} is x-coordinate of point cr and θ_{max} is the maximum rotation for the leading-edge of the airfoil as shown in Fig. 2. Note that only y-coordinate of point P is changed, and we do not change x_N; therefore $x_N = x_P$. Thickness of the deflected airfoil as a function of x-coordinate must be equal to that of original airfoil to define lower and upper surfaces of the airfoil. This type of airfoil deformation or nose drooping results in formation of a smooth airfoil geometry which is crucial in airfoil design.

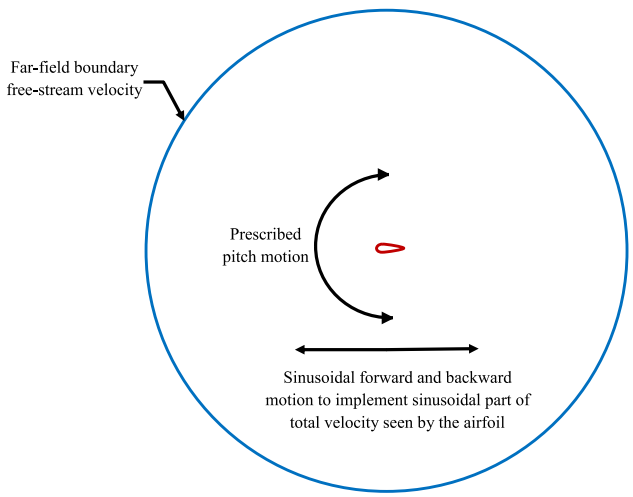

Fig. 4 Implementation of variable flow Mach number on the pitching airfoil

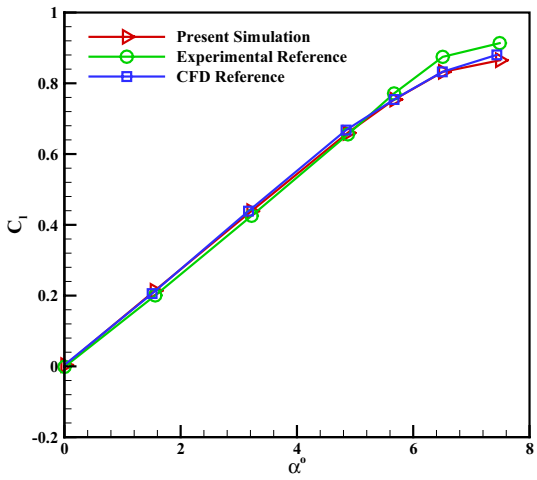

Fig. 6 Lift coefficient vs. angle of attack: comparison with experimental data and numerical results of Ref. [12] at $M = 0.6$ and $\alpha = 6.48°$ (static airfoil)

Two-dimensional grid used in this study consists of structured and unstructured parts. Structured part of the grid covers a layer over the airfoil to provide an appropriate orthogonal grid for the solution of viscous flow. For grid independence study, flow field around pitching airfoil at variable flow Mach number is simulated. Mach number of free-stream is set equal to the Mach number of flow along the blade section at $r/R = 0.865$ of the rotor blade of UH-60A helicopter while the helicopter is flying forward with $M_\infty = 0.21$ and $\mu = 0.33$. Aerodynamic coefficients of C_l and C_d of this case obtained on four grids with different densities including 109, 154, 188 and 217 thousand cells approximately are compared with each other. These grids have 600, 800, 1000 and 1200 nodes on the airfoil surface, respectively. Details of these grids are presented in Table 1 for both structured and unstructured regions. In all cases, structured grid extends at least to $0.07c$ away from the airfoil surface to make sure that viscosity effects remain in the structured part of the grid even if the airfoil stalls.

Structured grid around airfoil nose and tail are shown in Fig. 3a, b, respectively. Transition from structured to unstructured grid can be seen in Fig. 3c. Far-field boundary is set at $20c$ far from the airfoil, where gradients of flow properties diminish. Spalart–Allmaras turbulence model requires $y^+ \sim 1$ at the walls. This criterion is met by setting first node of the grid at a distance equal to $4.0 \times 10^{-6}c$ far from the wall.

Comparison of results obtained on these grids showed that results on grids denser than 188,000 cells with 1000 nodes on the airfoil surface do not change noticeably. Therefore this grid, called Grid-III, or grids with the same order of density will be chosen for dynamic simulations in present work. In all of the simulated cases, general details of generated grids are similar to that of Grid-III, and only the number of grids may change slightly.

Free-stream flow velocity seen by rotor blade section in forward flight of helicopter is variable by time. Since flow is simulated two-dimensionally, instantaneous component of free-stream velocity along the blade section should be determined. Due to rotation of blade, this component varies sinusoidally with time. Total free-stream velocity seen by the blade section is the sum of the abovementioned velocity component with the rotational speed of blade at that section. Note that helicopter blade airfoil is also in a pitch motion. These time variable motions are implemented using zone motion technique of ANSYS Fluent Software. As seen in Fig. 4, to implement sinusoidal part of total velocity seen by the airfoil, whole 2-D grid is moved forward and backward sinusoidally. At the far-field boundary free-stream velocity is set equal to the rotational speed of the blade at the section in question. Pitch motion of the blade section is implemented by prescribing rotation of the whole 2-D grid about 1/4th of airfoil chord. In this study, dynamic mesh deformation is prevented due to high amplitude of these motions.

As about time step, simulations were performed for different time steps to achieve solution convergence. As a result, it was found that time step of 1.2×10^{-5} s is appropriate. Details of time independence study will be discussed at the end of Sect. 5.

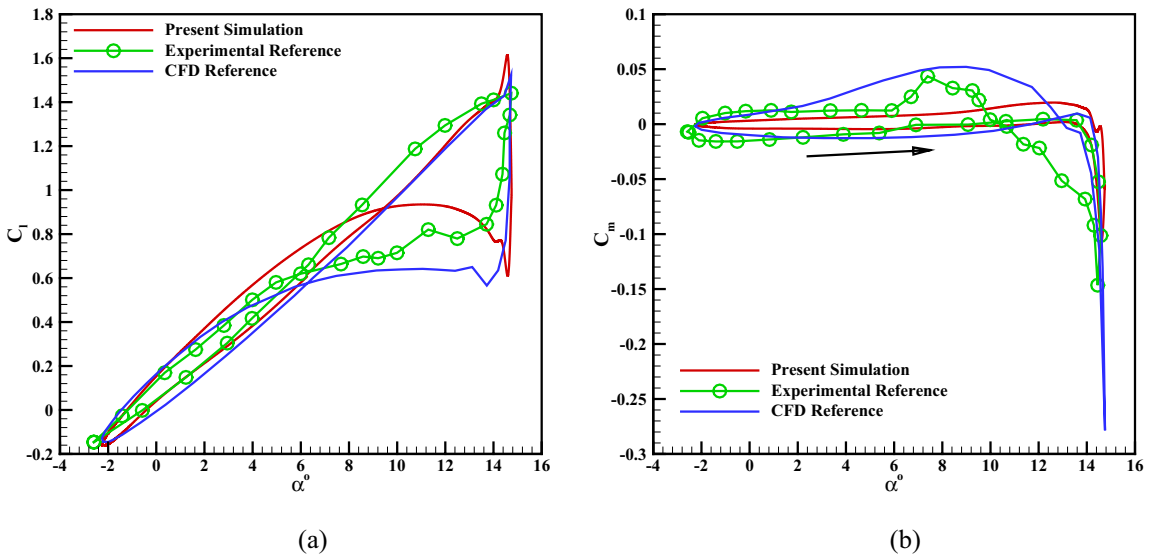

Fig. 7 Numerical results compared with experimental [42] and numerical [19] references for the pitching airfoil: **a** lift coefficient, **b** moment coefficient

4 Validation and verification

4.1 Static airfoil

In this section, numerical simulation is validated. For this purpose, stationary NACA-0012 airfoil is considered in flow with $M = 0.6$, $Re = 3 \times 10^6$ and $\alpha = 6.48°$, which is counted as high angle of attack for this Mach number. Experimental data and numerical results of C_P and $C_l - \alpha$ of this airfoil are given in Ref. [12]. This flow condition is close to the extreme conditions that occurs in the unsteady case of present research which includes local supersonic flow, shock wave and shock wave induced reverse flow. Therefore, it is an excellent candidate for validation purpose.

A grid with the quality of Grid-III and its order of density is used for this simulation. Number of cells required in this case to achieve results independent of grid density is found to be 191,000. As mentioned in Sect. 3, distance of the first node from airfoil surface in present study is about of $4.0 \times 10^{-6}c$; this is half of the value used in the structured O-type grid of Ref. [12]. Note that with this distance y^+ of about 1 is achieved on the airfoil. Pressure coefficient (C_P) along the airfoil surface is compared with C_P of the experiment and numerical simulation of Ref. [12] in Fig. 5. As it can be seen in Fig. 5, very good agreement is achieved. Especially, sudden rise of pressure coefficient in the leading-edge, shock wave location and shock strength. Lift coefficients (C_l) for several angles of attack are compared with those of experimental data and numerical results in Fig. 6. Agreement is excellent except in nonlinear angles of attack where, of course, errors are not more than 5.3% and 1.6% in comparison to experimental data and numerical results, respectively. Error with experiment is due to a small reverse flow region that is caused by a shock wave formed at the airfoil nose. In Ref. [12], algebraic eddy viscosity turbulence model is used. We believe that the difference between two numerical results in nonlinear angles is due to the different turbulence models used by Ref. [12] and present work. It should be noted that these angles of attack are considered high for Mach number of $M = 0.6$ creating complex flow structure that is more complex than the worst case happening in the main unsteady case studied in this research.

4.2 Pitching airfoil

Next case is NACA-0012 airfoil pitching about $\alpha = 6.25°$ angle of attack with amplitude of 8.5° in turbulent flow at $M = 0.4$ and $Re = 3.4 \times 10^6$. Lift and moment coefficients of present study are compared with those of experimental data [42] and numerical results [19] in Fig. 7. This case is simulated on the same grid described in previous Sect. 4.1.

Lift and moment coefficients are compared in Fig. 7a. On the upstroke, where most of the flow does not include reverse flow, results are in good agreement with the numerical results in the Ref. [19]. Compared to the experiment data, C_l is underpredicted by numerical simulations of present work and Ref. [19], especially at higher angles of attack. Angle of attack at which dynamic stall and extremes of aerodynamic coefficients at this angle occur is the essential parameter that is studied in the literature. Present numerical simulation predicts stall angle at about $\alpha = 14.6°$ which in comparison to 14.7° predicted by experimental data and numerical results of Ref. [19] includes negligible error of 0.68%. From Fig. 7a, $C_{l,max}$ is predicted 11.8% and 6.1% higher than that of the experimental and numerical references, respectively. Because of the vortex forming on the upper surface of the airfoil leading-edge, an overshoot in C_l is seen in both numerical results. Due to the different numerical schemes used by present work and Ref. [14], amounts of overshoots

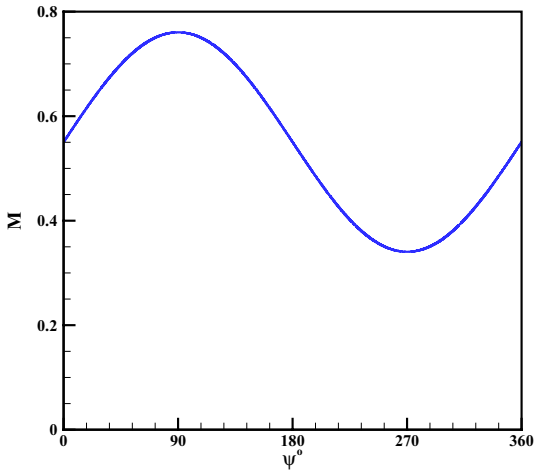

Fig. 8 Free-stream Mach number seen by the blade section along its camber at $r/R = 0.865$, $M_\infty = 0.21$ and $\mu = 0.33$

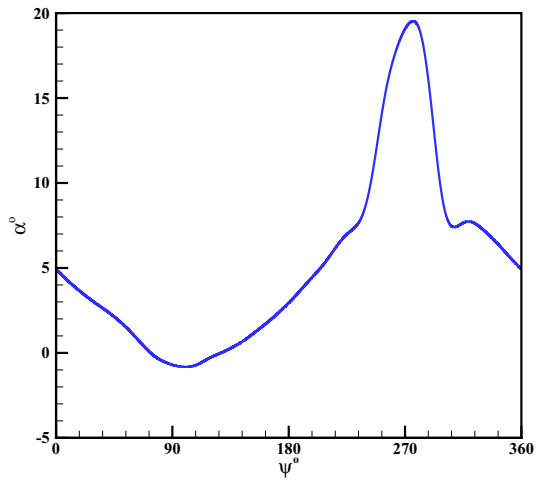

Fig. 9 Blade section angle of attack at $r/R = 0.865$, $M_\infty = 0.21$ and $\mu = 0.33$, predicted by the CAMRAD II code [36]

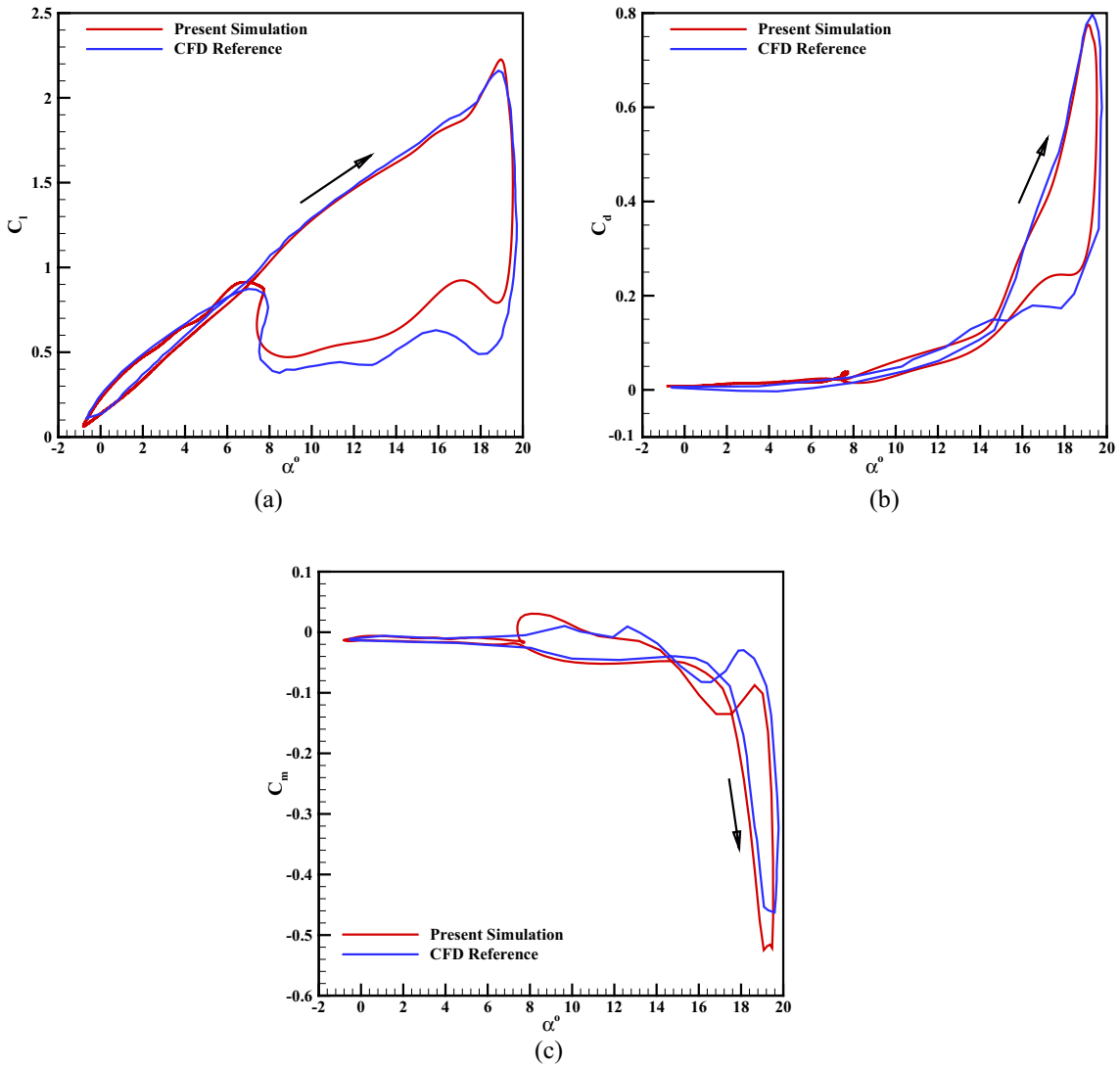

Fig. 10 Comparison of calculated aerodynamic coefficients of SSC-A09 airfoil with variable flow Mach and prescribed angle of attack with those of Ref. [19]: **a** lift, **b** drag and **c** moment

are not the same. From Fig. 7b, $C_{m,min}$ predicted by present simulation and that of Ref. [19] have 28% and 90% errors in comparison to the experimental data, respectively. This shows that during leading-edge vortex movement toward the trailing-edge, C_m cannot be predicted well using numerical simulations. Still, present study has produced better results compared to the numerical reference. On the downstroke, while the angle of attack decreases from its maximum, airfoil is still in deep stall, and reverse flow is dominant on the upper surface of the airfoil. This makes flow prediction very difficult for numerical simulations which use Reynolds-averaged turbulence modeling. It is important to note that even aerodynamic coefficients obtained from experimental data in deep stall angles do not match each other exactly in repetitious experiments. Good agreement is observed between present results and those of experimental data on the upstroke from low to high angles of attack of about 13°. As described above any comparison at high angles of attack on the downstroke is not valid. But as it is seen present results are in fairly good agreement with experimental data at lower angles of attack.

4.3 Pitching airfoil in variable flow Mach

In this section, results of a pitching SSC-A09 airfoil in a free-stream with variable flow Mach are verified with the numerical results of Kreho [19]. Free-stream Mach number is set equal to the Mach number of flow along the camber of blade section at $r/R = 0.865$ of the rotor blade of UH-60A helicopter while the helicopter is flying forward

with $M_\infty = 0.21$ and $\mu = 0.33$. Variation of free-stream Mach number versus azimuth angle for the blade section at $r/R = 0.865$ is plotted in Fig. 8 for one cycle; note that at azimuth angle of $\psi = 0.0$ rotor blade passes over the tail of the helicopter.

Free-stream velocity seen by the blade section (airfoil) includes mean part, which is equal to the blade angular velocity, i.e., $r\omega$, and sinusoid part which is due to the helicopter forward velocity. Angle of attack for this blade section is retrieved from Ref. [36], in which a comprehensive rotorcraft analysis code of CAMRAD II [36] is used to predict angle of attack for one cycle; see Fig. 9. At azimuth angles of about 90° where Mach number is maximum, angle of attack is close to zero. On the other hand, at azimuth angles of about 270° where dynamic pressure is minimum, lift force has to be supported by the increase of angle of attack to values as high as 19.5°. Other than that, in most azimuth angles of the cycle angle of attack is kept less than 7° to prevent possible shock wave and its induced reverse flow.

Aerodynamic coefficients are compared with those of Kerho's numerical results [19]. Grid-III, with 188,000 cells, with its details mentioned in Sect. 3 is used for this case. Similar to Ref. [19], one-equation Spalart–Allmaras turbulence model is used here.

As shown in Fig. 10a, C_l changes linearly with the angle of attack on the upstroke until $\alpha = 15°$. This linear behavior is due to lack of any reverse flow on the airfoil. As seen, present results follow those of Ref. [19] very well. A small difference starts to grow from $\alpha = 15°$ on the upstroke. At this angle of attack, vortex forms at the leading-edge and moves downstream; as a result some parts of the airfoil's upper surface are exposed to reverse flow. As the airfoil pitches upward this vortex grows up and covers more areas of the upper surface. At about $\alpha = 19°$, leading-edge vortex separates from the airfoil and puts the airfoil in deep stall. As shown in Fig. 10a, $C_{l,max}$ and the angle at which C_l stalls (α_{ls}) are predicted well compared to the results of Ref. [19]. Present $C_{l,max}$ is over predicted by about 3% but α_{ls} is predicted at 19.1° which is equal to the one predicted by Ref. [19]. Noticeable difference in the C_l in the deep stall during downstroke is due to the several attached and detached vortices in the flow above the upper surface of the airfoil. Note that the nature of these vortices is random and changes from cycle to cycle. Therefore, energies and locations of them cannot be predicted consistently by numerical simulations. This is why it cannot be expected to match numerical results with each other in deep stall conditions. Comparison of drag coefficient is demonstrated in Fig. 10b. It is shown that present C_d curve on the upstroke follows that of Ref. [19] very well. In the present study, angle at which drag peak happens is predicted equal to $\alpha = 19.1°$, which is about 1% less than that of Ref. [19]. Again $C_{d,max}$ is predicted very well; its value is only about 2.8% less than that predicted by Ref. [19]. On the upstroke, C_d increase diverges with the onset of leading-edge vortex formation at the angle of about 15.0°, and then it falls with the beginning of deep stall. According to Fig. 10c, moment coefficient is in good agreement with that of Ref.

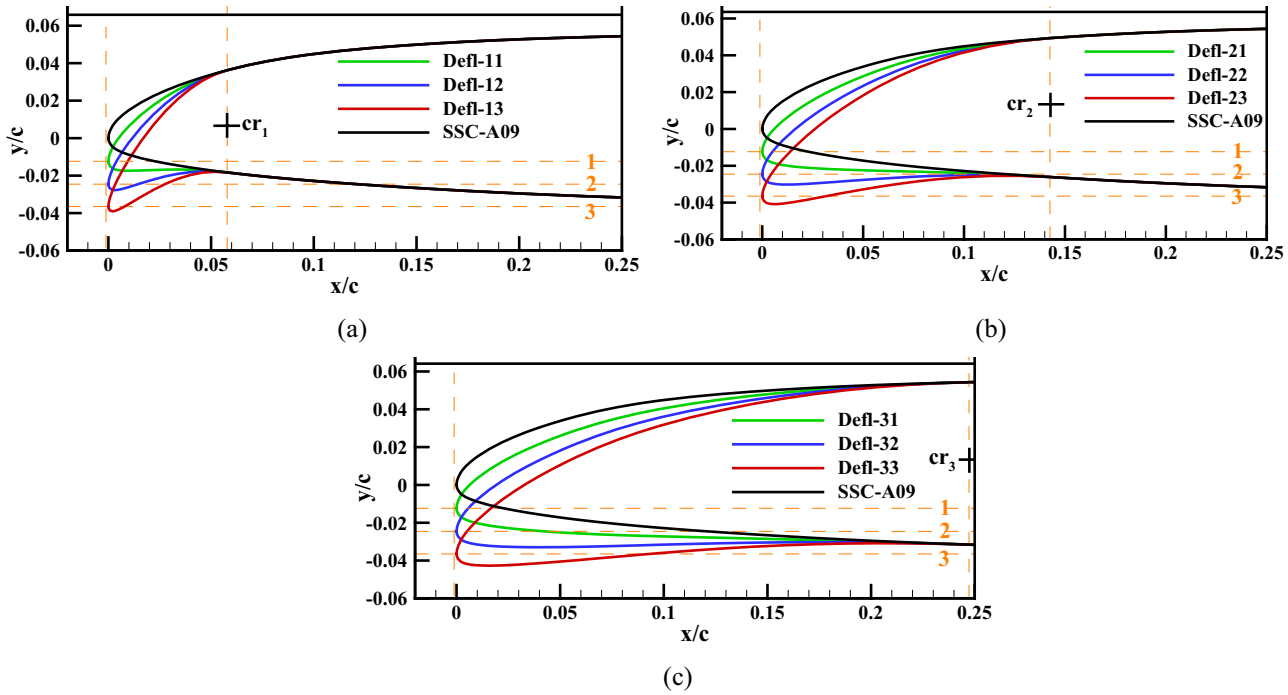

Fig. 11 Deformed airfoils: **a** Defl-1x airfoils with the center of rotation at $x/c = 0.058$, **b** Defl-2x airfoils with the center of rotation at $x/c = 0.143$ and **c** Defl-3x airfoils with the center of rotation at $x/c = 0.247$

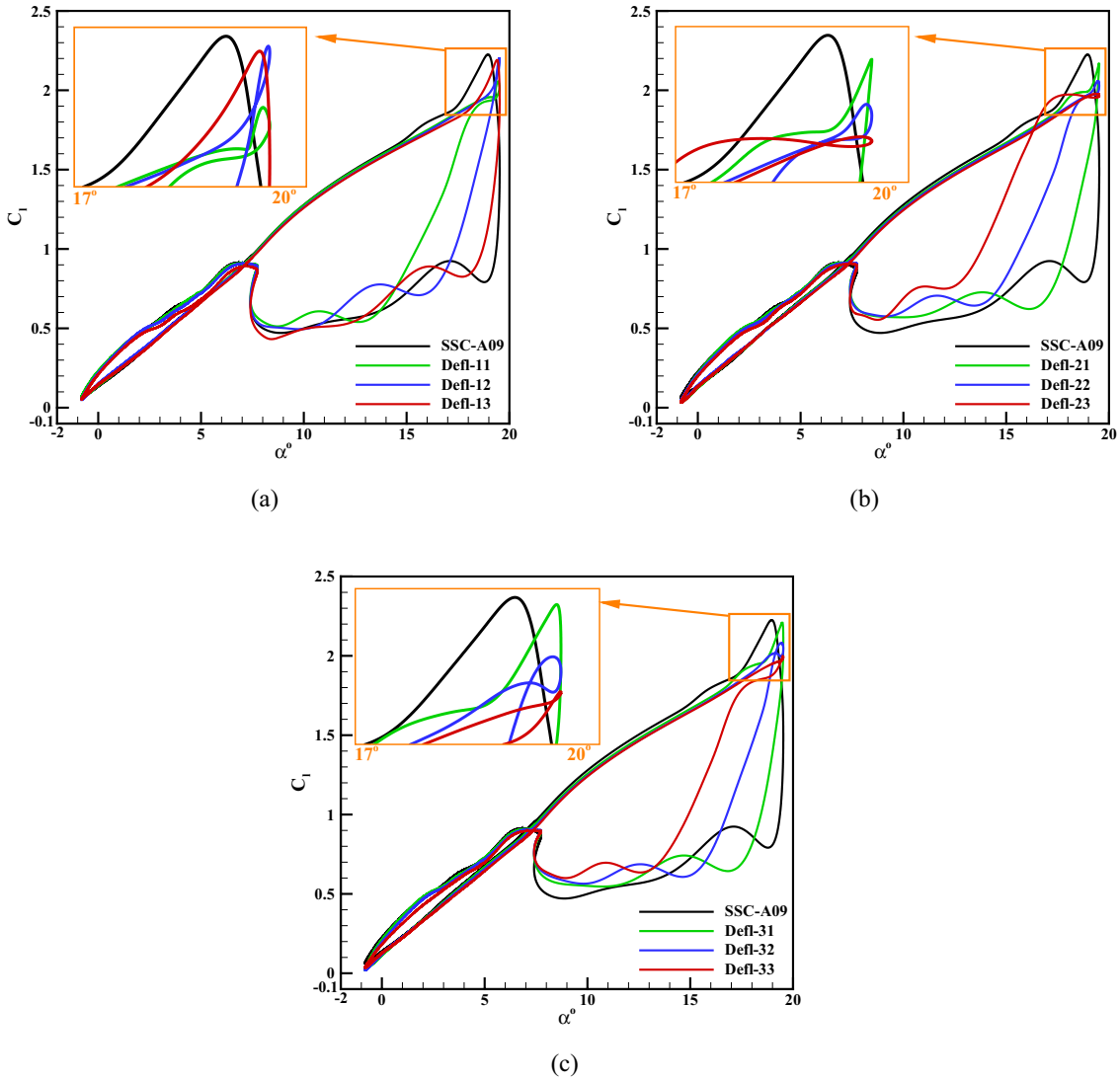

Fig. 12 Variation of C_l with angle of attack for drooped airfoils and original SSC-A09 pitching airfoil in variable flow Mach at $r/R = 0.865$, $M_\infty = 0.21$ and $\mu = 0.33$. **a** C_l results of Defl-1x and original airfoils, **b** C_l results of Defl-2x and original airfoils and **c** C_l results of Defl-3x and original airfoils

[19] on the upstroke. Note that C_m is highly dependent on the position of moment center. Therefore, as the position of the moment center in Ref. [19] is not known, small differences in C_m results are expected. In comparison to Ref. [19], angle at which moment coefficient drops sharply has been predicted excellently with a negligible error of 0.25%. Finally, it is worth to mention that this angle is independent of the location of the moment center.

Attention should be paid to the behavior of drag and moment coefficients. Absolute values of these two coefficients increase due to the growth of leading-edge vortex, which is not desirable. This is why the goal of researchers is to eliminate or reduce effects of the leading-edge vortex.

Comparison of results in three cases discussed in this section proves that present simulation is capable of simulating flow fields in this category and will result in predictions with little errors in the order of those that exist in the literature.

5 Results and discussion

In this study, a method is proposed to droop the nose of airfoil for dynamic stall reduction and alleviation. Present method is applied to the case of SSC-A09 pitching airfoil of UH-60A helicopter blade section in variable flow Mach at $r/R = 0.865$, $M_\infty = 0.21$ and $\mu = 0.33$ with variable angle of attack defined by Ref. [36]. Note that in all unsteady cases results after third cycle fitted those of the second cycle perfectly. Kerho [19] has mentioned also that 2.5 cycles are enough to achieve periodic convergence.

This case has been simulated by Kerho [19]. In his work, airfoil nose deflects dynamically as a function of blade rotation. Implementation of this rapid change of geometry is not easy in practice. In addition, it requires a sophisticated control system which adds weight to the blade structure. Although detail of the geometric airfoil deformation is not mentioned by Kerho [19], it is possible to achieve his deformed airfoil by the two geometric parameters presented in his paper.

In present study, drooping of the airfoil nose has been implemented by two different geometric parameters x_{cr} and θ_{max}, as introduced in Sect. 3. In present work, three values of x_{cr}/c equal to 0.058, 0.143 and 0.247 are studied. For each x_{cr}, three θ_{max} are examined based on values of $y_{L.E.}/c$ equal to − 0.0124, − 0.0246 and − 0.0365; note that $\tan(\theta_{max}) = y_{L.E.}/x_{cr}$. Therefore, nine cases will be investigated here, which cover an appropriate range of airfoil deformations. With this definition, effect of center of rotation coordinate on dynamic stall can be studied for each $y_{L.E.}$. These nine deformed airfoils are denoted by a two-digit index. First digit indicates center of rotation x_{cr}, and second digit determines $y_{L.E.}$. For example, Defl-13 is the airfoil deformed from $x_{cr}/c = 0.058$ for the leading-edge at $y_{L.E.}/c$ equal to − 0.0365. These 9 deformed airfoils are shown in Fig. 11.

Aerodynamic coefficients of deflected airfoils are plotted with respect to the angle of attack during one complete cycle of blade rotation in comparison to each other and the original airfoil in Fig. 12. It is shown in Fig. 12a–c that all the airfoils have successfully changed $C_{l,max}$ and alleviated α_{ls} more or less. Having examined C_l curves of Fig. 12 in detail, it can be observed that nose droop has alleviated α_{ls} but has reduced $C_{l,max}$. It is worth to mention that the main goal of dynamic stall control is to delay or alleviate stall angle α_{ls}. Delay of α_{ls} to even downstroke angles significantly prevents loss of airfoil lift during the whole cycle. Sudden rise of C_l which leads to a peak, called $C_{l,max}$, increases total lift of airfoil. However, this behavior indicates that a strong vortex has been formed in the leading-edge of airfoil which quickly results in dynamic stall. Therefore, much credit cannot be given to airfoils that increase merely the peak of C_l in a small region. Among all drooped airfoils in Fig. 12a, Defl-11 airfoil has alleviated stall angle α_{ls} more than others and even to the downstroke angles. Elimination of $C_{l,max}$ peak region in this airfoil shows that stall has occurred due to the vortex formation in the airfoil trailing-edge. As it can be seen in Fig. 12b, c, better results have been achieved by other deflections. Best results are obtained by Defl-23 in Fig. 12b and by Defl-33 in Fig. 12c. Again in both cases C_l has dropped at the corresponding α_{ls} on the airfoil downstroke, and no serious stall has happend. It is noted that in Fig. 12b, c where x_{cr} is far enough from the leading-edge, drooping will generally weaken leading-edge vortex and therefore alleviates α_{ls}.

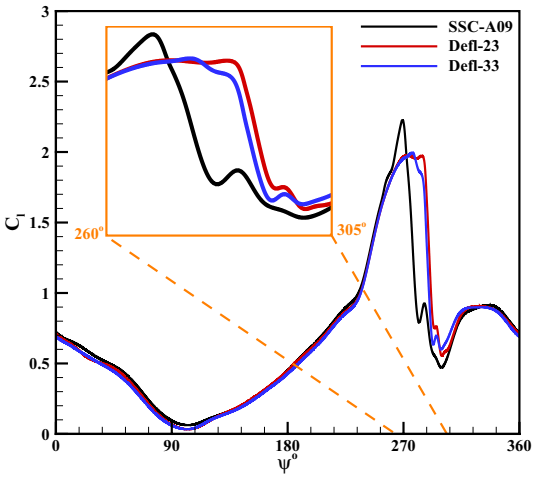

Fig. 13 Variation of C_l with azimuth angle for drooped airfoils and original SSC-A09 pitching airfoil in variable flow Mach at $r/R = 0.865$, $M_\infty = 0.21$ and $\mu = 0.33$

Table 2 Averages of C_l over a cycle for Defl-23, Delf-33 and original SSC-A09 airfoils in variable flow Mach at $r/R = 0.865$, $M_\infty = 0.21$ and $\mu = 0.33$

No	Airfoil type	Average of C_l	Improvement percentage*
1	SSC-A09	0.643	–
2	Defl-23	0.669	4.04
3	Defl-33	0.655	1.87

*With respect to that of the SSC-A09 airfoil

In general, results of Defl-23 and Defl-33 are similar to each other, but as seen in Fig. 13 in which C_l is plotted versus azimuth angle, the area under C_l curve of Defl-23 is slightly higher than that of Defl-33. Averages of C_l curves presented in Fig. 13 over a cycle are calculated and listed in Table 2 to show the superiority of Defl-23 and Defl-33 quantitatively. As seen, 4.04% enhancement in average of lift coefficient is achieved by Defl-23 airfoil which is our choice.

General trend of C_l behavior observed above can also be seen in C_d and C_m curves in Figs. 14 and 15, respectively. Having investigated C_d curves in Fig. 14, it can be shown that drooping the airfoil nose reduces $C_{d,max}$ very well. However in comparison to the original airfoil of SSC-A09, $C_{d,max}$ of Defl-23 and Defl-33 airfoils has the most reduction of 49.2% and 45.2%, respectively. Airfoil drooping also alleviates C_d

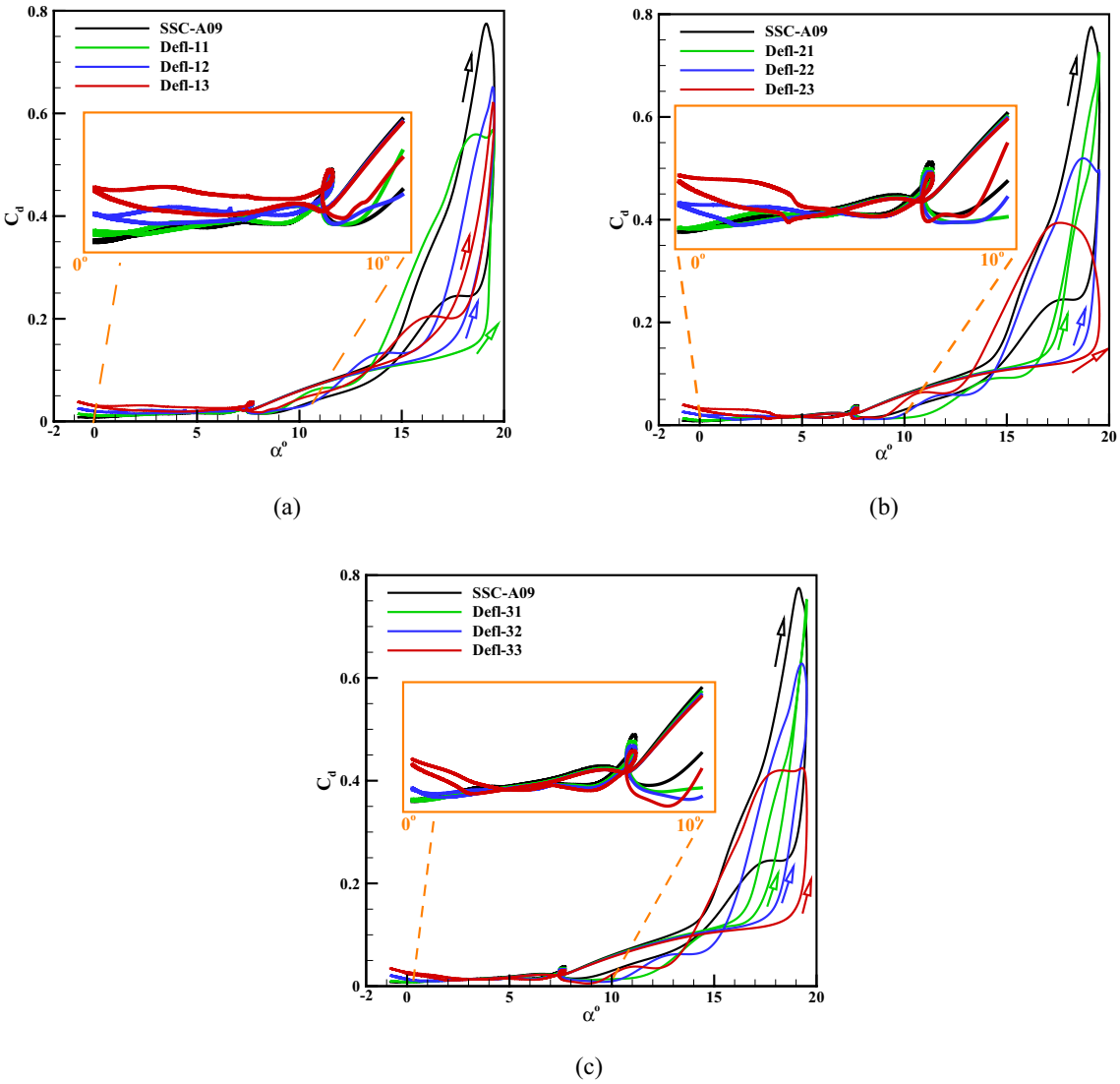

Fig. 14 Variation of C_d with angle of attack for drooped airfoils and original SSC-A09 pitching airfoil of in variable flow Mach at $r/R = 0.865$, $M_\infty = 0.21$ and $\mu = 0.33$. **a** C_d results of Defl-1x and original airfoils, **b** C_d results of Defl-2x and original airfoils and **c** C_d results of Defl-3x and original airfoils

sharp rise on the upstroke. This can be observed by comparing C_d curves of Defl-2x with each other in Fig. 14b and C_d curves of Defl-3x with each other in Fig. 14c. In these figures, Defl-23 and Defl-33 airfoils have the best alleviations. Although as can be seen Defl-23 alleviates C_d sharp rise slightly more than that of Defl-33. Again, it can be seen that in terms of drag characteristics Defl-23 airfoil performs better than Defl-33 airfoil.

At lower angles of attack, drag coefficients of the deflected airfoils are negligibly higher than that of original airfoil. However, noticeable reductions in $C_{d,max}$ are achieved by the deflected airfoils, especially by Defl-23. This completely satisfies overall superiority of proposed airfoils over the original airfoil.

In Fig. 15, moment coefficient, C_m, of drooped airfoils and the original airfoil of SSC-A09 are compared with each other. Here, we would like to decrease negative value of $C_{m,min}$ and alleviate sharp drop of C_m. Analysis of curves given in Fig. 15 is similar to that was done for C_d presented above with the fact that here decrease of negative value $C_{m,min}$replaces decrease of $C_{d,max}$ in the above analysis. As it can be seen, again airfoil with Defl-23 and Defl-33 has

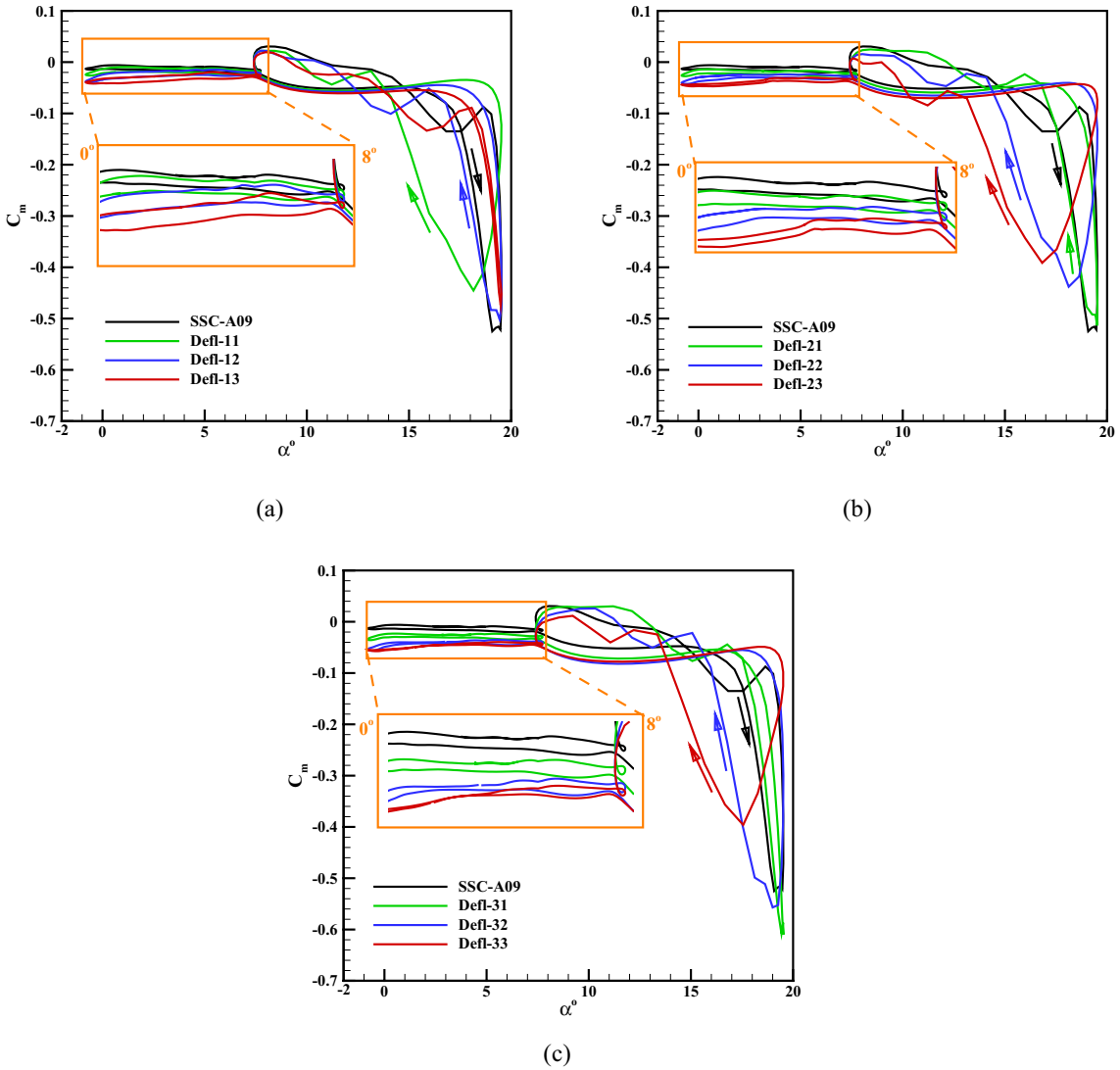

(a) (b) (c)

Fig. 15 Variation of C_m with angle of attack for drooped airfoils and original SSC-A09 pitching airfoil in variable flow Mach at $r/R = 0.865$, $M_\infty = 0.21$ and $\mu = 0.33$. **a** C_m results of Defl-1x and original airfoils, **b** C_m results of Defl-2x and original airfoils and **c** C_m results of Defl-3x and original airfoils

Table 3 Main results of the nine deflected and original SSC-A09 airfoils in variable flow Mach at $r/R = 0.865$, $M_\infty = 0.21$ and $\mu = 0.33$

No.	Airfoil type	α°_{ls}	$C_{l,max}$	$C_{d,max}$	$C_{m,min}$
1	SSC-A09	19.1	2.23	0.77	− 0.52
2	Defl-11	19.5	2.06	0.57	− 0.44
3	Defl-12	19.5	2.2	0.65	− 0.5
4	Defl-13	19.4	2.19	0.62	− 0.47
5	Defl-21	19.5	2.17	0.72	− 0.51
6	Defl-22	19.46	2.06	0.52	− 0.44
7	Defl-23*	19.5	1.98	0.39	− 0.39
8	Defl-31	19.47	2.21	0.75	− 0.61
9	Defl-32	19.5	2.08	0.63	− 0.56
10	Defl-33	19.5	1.99	0.42	− 0.39

*Deflected airfoil selected in this study

the most alleviated sharp drop of C_m and decrease of negative $C_{m,min}$. Defl-33 performs slightly better than Defl-23 in terms of alleviation of C_m sharp drop; although approximately the same $C_{m,min}$ is observed. But note that regarding to superior results of Defl-23 in lift and drag coefficients, this airfoil is the final selection.

Results of C_m show that airfoil drooping slightly increases negative C_m undesirably in low angles of attack where Mach number is high. We note that cambered airfoils generate negative pitching moment at low angles of attack with respect to low cambered or symmetric airfoils. In the present work, nose drooping increases airfoil camber with respect to that of the original one. Therefore at low angles of attack, slightly higher negative pitching moment is observed for deflected airfoils. Although it is

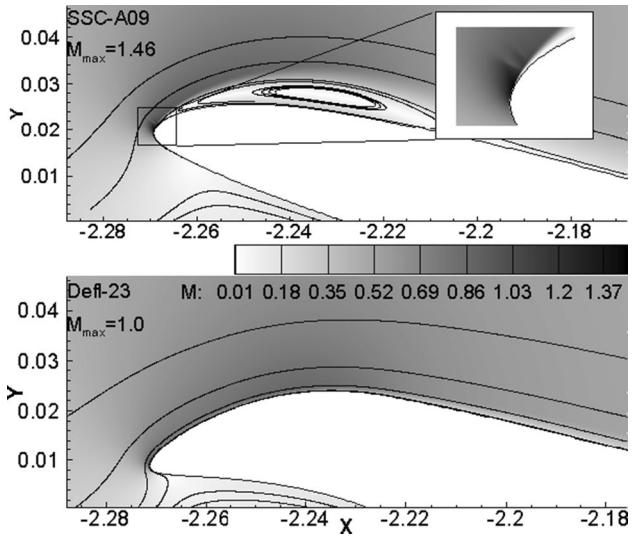

Fig. 16 Streamlines and Mach contours near the airfoil nose for original SSC-A09 and deformed Defl-23 airfoils at $r/R = 0.865$, $\psi = 225°$, $M_\infty = 0.21$, $\alpha = 15.2°$ and $\mu = 0.33$.

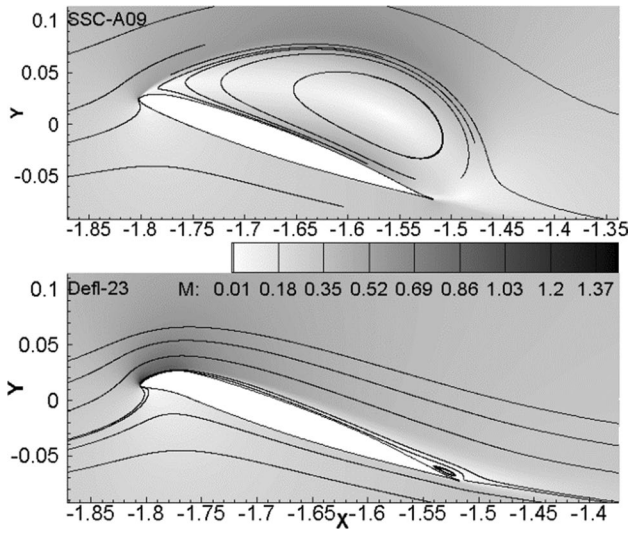

Fig. 17 Streamlines and Mach contours near the airfoil nose for original SSC-A09 and deformed Defl-23 airfoils at $r/R = 0.865$, $\psi = 270°$, $M_\infty = 0.21$, $\alpha = 19.12°$ and $\mu = 0.33$.

preferred to keep C_m near zero, always some compromises should be made in the design process.

To have an overall view over improvements gained by the deflected airfoils, the main results of Figs. 12, 14 and 15 including α_{ls}, $C_{l,max}$, $C_{d,max}$ and $C_{m,min}$ for deflected and original SSC-A09 airfoils are presented in Table 3.

Since Defl-23 airfoil has the best overall performance among other candidates, streamlines and Mach contours are plotted for SSC-A09 and Defl-23 airfoils in Fig. 16 at the azimuth angle of $\psi = 225°$, where $\alpha = 15.2°$. As it can be seen in this figure, adverse pressure gradient due to the shock wave at the upper surface of SSC-A09 nose results in reverse flow with a vortex. Such a vortex has not been formed on the nose of Defl-23 airfoil. Note that Mach number around the nose of this airfoil has not gone above 1.0. Nose vortex and its move toward the trailing-edge is the reason of nonlinear increase and overshoot of C_l, sharp rise of C_d and sudden drop of C_m.

In Fig. 17, streamlines and Mach contours are plotted for the SSC-A09 and Defl-23 airfoils at azimuth angle of $\psi = 270°$ where $\alpha = 19.12°$. At this stage, the leading-edge vortex covers all upper surface of the original SSC-A09 airfoil. Therefore, this airfoil has entered deep stall. For the Defl-23 airfoil, however no leading-edge reverse flow has been formed yet. As can be explored from Fig. 13, airfoil Defl-23 enters deep stall at azimuth angle of about $\psi = 287°$.

Analysis presented above is for spanwise section of $r/R = 0.865$ for the rotor speed of 391.7 RPM. It was shown that the advantage of proposed Defl-23 airfoil over SSC-A09 airfoil was to alleviate deep stall. Here, our intention is to analyse performance of these two airfoils for another blade section at $r/R = 0.7$ which experiences lower rotational velocity at the same free-stream condition of $M_\infty = 0.21$ and advance ratio of $\mu = 0.33$. As will be shown, Defl-23 airfoil interestingly eliminates dynamic stall at this radius. Note that the only change in flow simulation would be its free-stream mean velocity seen by the blade section.

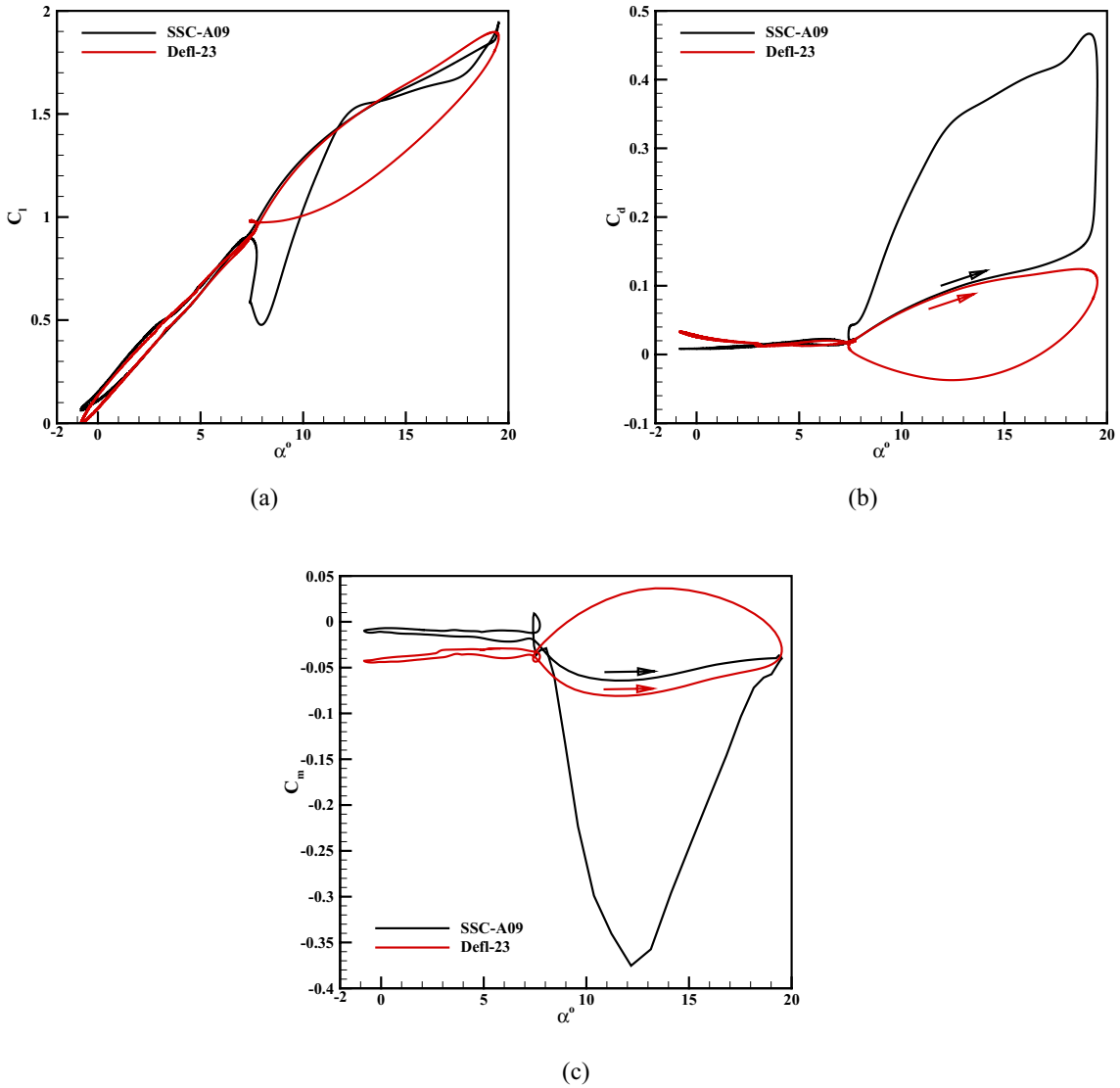

Fig. 18 Aerodynamic coefficients variation with angle of attack for Defl-23 airfoil and original SSC-A09 pitching airfoil in variable flow Mach at $r/R = 0.7$, $M_\infty = 0.21$ and $\mu = 0.33$: **a** lift, **b** drag and **c** moment coefficients

Table 4 Main results of Delf-23 and original SSC-A09 airfoils in variable flow Mach at, and

No.	Airfoil type	α°_{ls}	$C_{l,max}$	$C_{d,max}$	$C_{m,min}$
1	SSC-A09	19.5	1.94	0.46	-0.37
2	Defl-23	19.5	1.9	0.12	-0.08

By mean velocity reduction, compressibility effects relating to the Mach number become less critical. For both Defl-23 and original airfoils, aerodynamic coefficients of C_l, C_d and C_m are plotted in Fig. 18a–c, respectively. Examination of C_l curves reveals that although with respect to blade section at radius of $r/R = 0.865$, dynamic stall has been delayed on SSC-A09 airfoil, it is not eliminated. As seen in Fig. 18a, only light stall [10] has occurred on Defl-23 airfoil during its downstroke. This is because leading-edge vortex did not form at all on the airfoil as was observed by the authors. As about C_d, it is obvious that sharp rise of C_d and its peak value of $C_{d,max}$ in SSC-A09 airfoil is eliminated by the proposed Delf-23 airfoil in Fig. 18b. In addition average drag during a cycle that is determined by area under C_d curve is dramatically reduced by the proposed airfoil. Examination of Fig. 18c shows that with the proposed Delf-23 airfoil, drop of C_m and its negative peak value during downstroke in SSC-A09 airfoil is substantially eliminated by the proposed Delf-23 airfoil. C_m of present airfoil remains about zero with no sudden change. As results show, dynamic stall has been

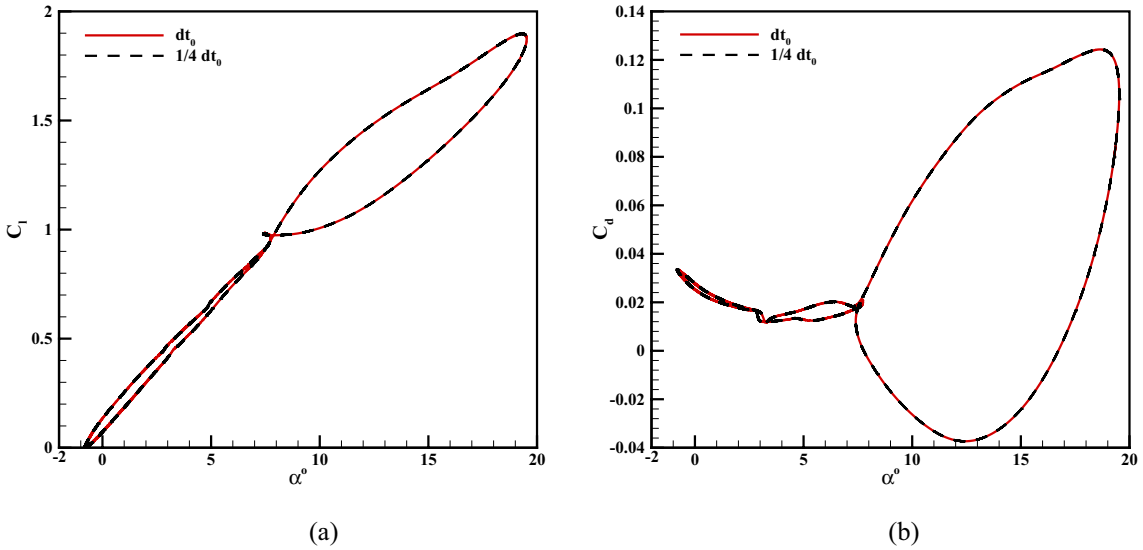

Fig. 19 Solution time independence study for Defl-23 pitching airfoil in variable flow Mach at $r/R = 0.7$, $M_\infty = 0.21$ and $\mu = 0.33$: **a** lift, **b** drag coefficients

definitely eliminated on proposed Delf-23 airfoil. Main results including α_{ls}, $C_{l,max}$, $C_{d,max}$ and $C_{m,min}$ obtained from Fig. 18 are presented in Table 4. It is worth to mention that elimination of dynamic stall in this study has been achieved with an efficient drooping and not with a complicated and expensive dynamic deflection proposed by others.

Time step independence study is done on lift and drag coefficients for the proposed deformed Defl-23 airfoil with variable flow Mach at $r/R = 0.7$ with $M_\infty = 0.21$ and $\mu = 0.33$. First, flow was simulated with the largest time step, called dt_0, that resulted in solution convergence. Then smaller time steps of $1/4dt_0$ was tried. As seen in Fig. 19, results of Defl-23 airfoil including aerodynamic coefficients of C_l and C_d fit each other during one whole cycle for both time steps mentioned above. With this process, time step of $1.2 \times 10^{-5}s$ was found to be appropriate.

6 Conclusions

In this study, flow field around helicopter blade section in forward flight is investigated numerically by solving 2-D viscous compressible Reynolds-averaged Navier–Stokes equations. The effect of forward flight speed is implemented in the two-dimensional model resulting in a time variable flow speed seen by the airfoil. Therefore phenomena such as shock wave near the leading-edge of airfoil, which has crucial role in the formation of dynamic stall are modeled according to the more realistic flow conditions. In this study, different airfoil nose drooping is examined, and it was shown that dynamic stall is reduced and alleviated using these deformed airfoils. This means that an airfoil can be drooped carefully to remove shock wave on its leading-edge. Therefore due to elimination of after-shock vortex, no dynamic stall will occur at this stage. Although dynamic stall may occur later due to trailing-edge reversed flow, its strength will be weaker, and therefore, C_d and C_m will not reach their extremes when dynamic stall forms due to leading-edge vortex.

Following conclusions can be made from present research:

1. Airfoil drooping proposed in this study can definitely alleviate dynamic stall to the angles on the downstroke, i.e., a delay of 16° from azimuth angle of $\psi = 270°$ to $\psi = 286°$.
2. Reduction of 49.2% in $C_{d,max}$ and 25% in absolute value of $C_{m,min}$.
3. Possible elimination of dynamic stall in cases where compressibility effects are not severe, as shown in this paper.
4. It was shown that dynamic stall alleviation can be achieved by permanent airfoil drooping, which does not impose design complexities and expenses needed for dynamic deformation of airfoils proposed by others.

Compliance with ethical standards

Conflict of interest The authors declare no potential conflicts of interest with respect to the research, authorship and/or publication of this article.

References

1. Lian Y, Ol M, Shyy W (2008) Comparative study of pitch-plunge airfoil aerodynamics at transitional reynolds number. In: 46th AIAA aerospace sciences meeting and exhibit, 2008, p 652
2. Chandrasekhara M, Wilder M, Carr L (1998) Competing mechanisms of compressible dynamic stall. AIAA J 36(3):387–393
3. Bousman WG (1998) A qualitative examination of dynamic stall from flight test data. J Am Helicopter Soc 43(4):279–295
4. Liiva J (1969) Unsteady aerodynamic and stall effects on helicopter rotor blade airfoil sections. J Aircr 6(1):46–51
5. Ham ND, Garelick MS (1968) Dynamic stall considerations in helicopter rotors. J Am Helicopter Soc 13(2):49–55
6. Mulleners K, Kindler K, Raffel M (2012) Dynamic stall on a fully equipped helicopter model. Aerosp Sci Technol 19(1):72–76
7. Geissler W, Haselmeyer H (2006) Investigation of dynamic stall onset. Aerosp Sci Technol 10(7):590–600
8. Šidlof P, Vlček V, Štěpán M (2016) Experimental investigation of flow-induced vibration of a pitch–plunge NACA 0015 airfoil under deep dynamic stall. J Fluids Struct 67:48–59
9. Jain R, Le Pape A, Grubb A, Costes M, Richez F, Smith M (2018) High-resolution computational fluid dynamics predictions for the static and dynamic stall of a finite-span OA209 wing. J Fluids Struct 78:126–145
10. Dumlupinar E, Murthy V (2011) Investigation of dynamic stall of airfoils and wings by CFD. In: 29th AIAA applied aerodynamics conference, 2011, p 3511
11. Ekaterinaris J (1989) Compressible studies on dynamic stall. In: 27th Aerospace sciences meeting, 1989, p 24
12. Visbal M (19988) Effect of compressibility on dynamic stall of a pitching airfoil. In: 26th aerospace sciences meeting, 1988, p 132
13. Ericsson L, Reding J (1984) Shock-induced dynamic stall. J Aircr 21(5):316–321
14. Sadr M, Badiei D, Shams S (2019) Developments of a semiempirical dynamic stall model for unsteady airfoils. J Braz Soc Mech Sci Eng 41(10):454
15. Singh C, Peake DJ, Kokkalis A, Khodagolian V, Coton FN, McD Galbraith RA (2006) Control of rotorcraft retreating blade stall using air-jet vortex generators. J Aircr 43(4):1169–1176
16. Geissler W, Dietz G, Mai H, Bosbach J, Richard H (2005) Dynamic stall and its passive control investigations on the OA209 airfoil section. In: 31st European Rotorcraft Forum, Florence, Italy
17. Al-Jaburi K, Feszty D (2018) Passive flow control of dynamic stall via surface-based trapped vortex generators. J Am Helicopter Soc 63(3):1–14
18. Ramesh K, Ke J, Gopalarathnam A, Edwards J (2012) Effect of airfoil shape and Reynolds number on leading edge vortex shedding in unsteady flows. In: 30th AIAA applied aerodynamics conference, 2012, p 3025
19. Kerho MF (2007) Adaptive airfoil dynamic stall control. J Aircr 44(4):1350–1360
20. Chandrasekhara M, Martin PB, Tung C (2004) Compressible dynamic stall control using a variable droop leading edge airfoil. J Aircr 41(4):862–869
21. Sahin M, Sankar LN, Chandrasekhara M, Tung C (2003) Dynamic stall alleviation using a deformable leading edge concept-a numerical study. J Aircr 40(1):77–85
22. Reuster J, Baeder J (2001) Leading edge deformation for dynamic stall control. In: 39th Aerospace sciences meeting and exhibit, 2001, p 120
23. Grohsmeyer S, Ekaterinaris J, Platzer M (1798) Numerical investigation of the effect of leading edge geometry on dynamic stall of airfoils. In: 22nd fluid dynamics, plasma dynamics and lasers conference, 1991, p 1798
24. Kral L, Donovan J, Cain A, Cary A, Kral L, Donovan J, Cain A, Cary A (1997) Numerical simulation of synthetic jet actuators. In: 4th shear flow control conference, 1997, p 1824
25. Carr L, McAlister K (1983) The effect of a leading-edge slat on the dynamic stall of an oscillating airfoil. In: Aircraft design, systems and technology meeting, 1983, p 2533
26. Zanotti A, Gibertini G (2018) Experimental assessment of an active L-shaped tab for dynamic stall control. J Fluids Struct 77:151–169
27. McCloud III JL, Hall LP, Brady JA (1960) Full-scale windtunnel tests of blowing boundary-layer control applied to a helicopter rotors
28. Wang Q, Zhao Q, Wu Q (2015) Aerodynamic shape optimization for alleviating dynamic stall characteristics of helicopter rotor airfoil. Chin J Aeronaut 28(2):346–356
29. Benton SI, Visbal MR (2018) Effects of leading-edge geometry on the onset of dynamic stall. AIAA J 56(10):4195–4198
30. Niu J, Lei J, Lu T (2018) Numerical research on the effect of variable droop leading-edge on oscillating NACA 0012 airfoil dynamic stall. Aerosp Sci Technol 72:476–485
31. Zhao G-q, Zhao Q-j (2015) Dynamic stall control optimization of rotor airfoil via variable droop leading-edge. Aerosp Sci Technol 43:406–414
32. Babinsky H, Fernie R NACA0012 Aerofoil in an oscillating freestream. In: 40th AIAA Aerospace sciences meeting & exhibit, 2002, pp 2002–0115
33. Huang D, Li J, Liu Y (2015) Airfoil dynamic stall and aeroelastic analysis based on multi-frequency excitation using CFD method. Procedia Eng 99:686–695
34. Qijun Z, Yiyang M, Guoqing Z (2017) Parametric analyses on dynamic stall control of rotor airfoil via synthetic jet. Chin J Aeronaut 30(6):1818–1834
35. Fung K-Y, Carr L (1991) Effects of compressibility on dynamic stall. AIAA J 29(2):306–308
36. Johnson W (1998) Rotorcraft aerodynamics models for a comprehensive analysis. In: Annual forum proceedings-American helicopter society, 1998. American Helicopter Society, pp 71–94
37. Gharali K, Johnson DA (2013) Dynamic stall simulation of a pitching airfoil under unsteady freestream velocity. J Fluids Struct 42:228–244
38. Seyednia M, Masdari M, Vakilipour S (2019) The influence of oscillating trailing-edge flap on the dynamic stall control of a pitching wind turbine airfoil. J Braz Soc Mech Sci Eng 41(4):192
39. Spalart P, Allmaras S A one-equation turbulence model for aerodynamic flows. In: 30th aerospace sciences meeting and exhibit, 1992, p 439
40. Wang Q, Zhao Q (2018) Rotor airfoil profile optimization for alleviating dynamic stall characteristics. Aerosp Sci Technol 72:502–515
41. Blazek J (2015) Computational fluid dynamics: principles and applications. Butterworth-Heinemann, San Diego
42. Wood ME (1979) Results of oscillatory pitch and ramp tests on the NACA 0012 blade section. Aircraft Research Association Memo 220, UK